The microlayer framework: extension to aggregates with non-uniform shapes

Marcel May[1], **Ines Wollny**[1], **Jakob Platen**[1], and **Michael Kaliske**[1,*]

[1] Institute for Structural Analysis, Technische Universität Dresden, 01062 Dresden, Germany.

The microlayer framework is a novel, powerful method for the numerical simulation of heterogeneous materials, such as aggregate-matrix composites across different scales. While the framework has previously only been applied to geometrically isotropic aggregates, its mathematical formulation also enables the development of material models for aggregate-matrix composites with pronounced spatial directionality, an inherent characteristic of many materials in this class. In this work, a stepwise approach is adopted: first, simplified, non-uniformed shaped representative volume elements (RVEs) are studied to investigate their macroscopic behavior. Based on the limitations identified in this initial formulation, a refined RVE is then developed that satisfies both mathematical consistency and mechanical plausibility.

1 Introduction

A material model that incorporates non-uniform shaped aggregate geometries, instead of relying solely on idealized spherical inclusions embedded in a homogeneous matrix, offers significant advantages in realistically capturing the mechanical behavior of heterogeneous materials. Real-world microstructures often contain elongated, platelet-like, or irregularly shaped constituents, such as the flake-shaped mineral inclusions in asphalt mixtures, which significantly influence their directional stiffness and cracking behavior [1]. Similarly, natural soils exhibit inherent anisotropy due to sediment layering and particle alignment, which affects strength [2]. In fiber-reinforced polymers and biological tissues such as tendons or cortical bones, preferred fiber orientations govern the mechanical response and failure modes [3]. By accounting for such non-inform geometries, models can better simulate directional effects like crack propagation or localized plasticity. Recent micromechanical studies have demonstrated that using ellipsoidal or irregular-shaped inclusions result in more accurate predictions of macroscopic behavior in composites and geomaterials [4], making them essential tools for reliable material design and structural analysis. So far, the microlayer framework has been successfully applied to materials with uniform aggregate-matrix composites. For concrete, it was shown by employing a constitutive model with a damage formulation that anisotropic multiaxial stress states resulting from direction-dependent local damage can be represented more realistically than with previous formulations [5]. This work examines the requirements for non-uniform shaped aggregates within the microlayer framework to ensure both physical and mathematical plausibility, thereby providing modeling techniques suitable for multiscale approaches. This important extension has been missing so far. While previously the anisotropy of macroscopic material properties had to be generated through different material histories in the individual layers, it can now be prescribed a priori by the geometry. The analysis is restricted to single-particle systems in order to focus on aggregate geometry, however, multi-aggregate RVEs are equally feasible [5]. The structure of this work is as follows. First, the necessary mathematical and mechanical foundations of scale transfer within the microlayer framework are introduced in Section 2. Section 3 outlines the geometric requirements for potential RVE unit cells. Subsequently, in Section 4, the viscoelastic material model employed at the microstructural level is presented. In Section 5, numerical examples are used to demonstrate and discuss that geometric compliance alone is insufficient to yield physically meaningful macroscopic responses. Based on these insights, an optimized RVE is developed. Numerical investigations then show that this RVE is suitable as a representative element for non-uniform shaped aggregate-matrix composites, both from a mechanical and a mathematical perspective. The work discusses the conditions that must be met when creating a RVE for a specific target material. It concludes with an outlook on further optimization of the RVE geometry.

2 Microlayer framework

2.1 Deformation gradient and strain energy function

The solid body $\mathcal{B}$ under consideration is a subset of the three-dimensional Euclidean space $\mathbb{R}^3$. At the initial time $t = 0$, the body is assumed to be in its original, stress-free reference configuration, denoted by $\mathcal{B}_0$. As time evolves ($t > 0$), the body's current configuration is represented by $\mathcal{B}_t$. The motion of the body over time is described by the mapping $\boldsymbol{\varphi}_t : \boldsymbol{X} \rightarrow \boldsymbol{x}$. The deformation gradient $\boldsymbol{F}$ is defined as the derivative of this transformation. It characterizes how the displacement of material

* Corresponding author: e-mail michael.kaliske@tu-dresden.de

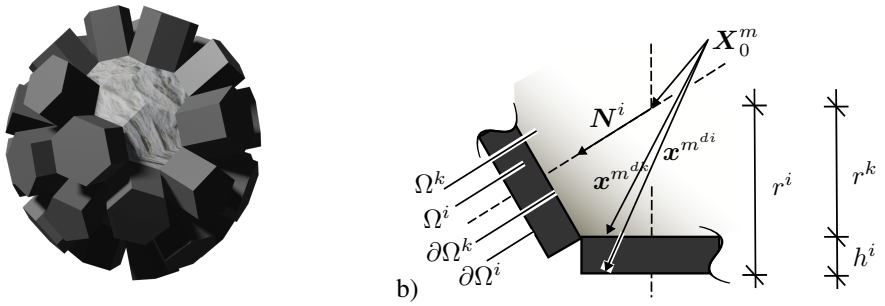

Fig. 1: a) Illustration of the shape of the RVE and b) geometry definition.

points within the body (given by $\boldsymbol{u}$) contributes to the overall change in shape, including any rigid body motions such as rotation, which are represented by the identity tensor $\boldsymbol{I}$

$$\boldsymbol{F} := \frac{\partial \boldsymbol{\varphi}_t}{\partial \boldsymbol{X}} = \mathrm{Grad}(\boldsymbol{\varphi}_t) = \mathrm{Grad}(\boldsymbol{u}) + \boldsymbol{I}. \tag{1}$$

To describe the stored elastic energy within the body $\mathcal{B}$, a strain energy density function ψ is introduced. For a homogeneous material, this energy function depends solely on the deformation gradient

$$\psi = \psi(\boldsymbol{F}). \tag{2}$$

In the context of the microlayer model introduced in this work, the transition to the macroscopic scale can be formulated using the first Piola–Kirchhoff stress tensor $\boldsymbol{P}$, which is energetically conjugate to the deformation gradient $\boldsymbol{F}$

$$\boldsymbol{P} = \frac{\partial \psi}{\partial \boldsymbol{F}}. \tag{3}$$

The corresponding material tangent tensor is then defined as

$$\mathbb{C}^{\boldsymbol{P}} = \frac{\partial \boldsymbol{P}}{\partial \boldsymbol{F}}. \tag{4}$$

2.2 Microlayer formulation

In this work, all geometries of the representative volume element (RVE) are characterized by an infinitely stiff aggregate Ω^k, which is connected at its surfaces i with thin but deformable homogeneous layers Ω^i of the height h^i. A suitable geometry can be seen in Figure 1. The domain Ω of the RVE results in

$$\Omega = \Omega^k \cup \bigcup_{i=1}^{n} \Omega^i. \tag{5}$$

The kinematics and geometry of the RVE are not chosen in isolation from the macroscale, but are a consequence of the application of the Principle of Multiscale Virtual Power (PMVP), a variational multiscale framework developed in [6]. For this purpose, kinematic insertion operators are first defined for the aggregate and the layers in order to obtain a relationship between the displacement fields of the micro level $\boldsymbol{u}^m$ and the macro level $\boldsymbol{u}^{\mathcal{M}}$. Due to the infinite rigidity of the aggregate, $\boldsymbol{u}^m_{\boldsymbol{x}^{m^k} \in \Omega^k}$ results from the macroscopic translations and rotations $\boldsymbol{R}^{\mathcal{M}}$ (strain-free component of the deformation gradient ($\boldsymbol{R} = \boldsymbol{F} \cdot \boldsymbol{U}^{-1}$)) around the geometric center $\boldsymbol{X}_0^m$

$$\boldsymbol{u}^m_{\boldsymbol{x}^{m^k} \in \Omega^k} = \underbrace{\boldsymbol{u}^{\mathcal{M}}}_{\text{translation}} + \underbrace{(\boldsymbol{R}^{\mathcal{M}} - \boldsymbol{1}) \cdot (\boldsymbol{x}^{m^k} - \boldsymbol{X}_0^m)}_{\text{rotation}}. \tag{6}$$

Assuming that the surface $\partial\Omega^i$ of the RVE remains parallel to the interface between the aggregate and the layer $\partial\Omega^k$, the displacement fluctuations $\tilde{\boldsymbol{u}}^m$ must vanish, because this surface is a symmetry plane. Displacement fluctuations are a central element of the PMVP. They describe the portion of the dispalcement field at the RVE level, which ensures equilibrium. The following therefore applies to the displacements on $\partial\Omega^i$

$$\boldsymbol{u}_{\boldsymbol{x}^{m^{di}} \in \partial\Omega^i} = \boldsymbol{u}^{\mathcal{M}} + (\boldsymbol{F}^{\mathcal{M}} - \boldsymbol{1}) \cdot (\boldsymbol{x}^{m^{di}} - \boldsymbol{X}_0^m). \tag{7}$$

A homogeneous displacement gradient is assumed for the displacement field $\boldsymbol{u}_{\boldsymbol{x}^{m^i} \in \Omega^i}$ of a layer i. Linear interpolation between the known displacement fields of the layer base and top surface results in

$$\boldsymbol{u}_{\boldsymbol{x}^{m^i} \in \Omega^i} = \boldsymbol{u}_{\boldsymbol{x}^{m^{dk}} \in \partial\Omega^k} f(\boldsymbol{x}^{m^i}) + \boldsymbol{u}_{\boldsymbol{x}^{m^{di}} \in \partial\Omega^i} [1 - f(\boldsymbol{x}^{m^i})] \tag{8}$$

with

$$f(\boldsymbol{x}^{m^i}) = \frac{r^i}{h^i} - \frac{1}{h^i}(\boldsymbol{x}^{m^i} - \boldsymbol{X}_0^m) \cdot \boldsymbol{N}^i. \tag{9}$$

To derive the final expressions, it is assumed that coordinates $\boldsymbol{x}^{m^{di}}$ and $\boldsymbol{x}^{m^{dk}}$ are decomposed into radial and tangential components as proposed in [7]. To enforce a homogeneous strain state, tangential contributions are neglected. This allows the transformation of all displacement-determining radial components into linear relations, and results in the following kinematically consistent expression for the layer displacement field

$$\begin{aligned}\boldsymbol{u}_{\boldsymbol{x}^{m^i} \in \Omega^i} = \boldsymbol{u}^{\mathcal{M}} &+ (\boldsymbol{F}^{\mathcal{M}} - \boldsymbol{1}) \cdot (\boldsymbol{x}^{m^{di}} - \boldsymbol{X}_0^m) \\ &+ \left[\frac{r^i}{h^i} - \frac{1}{h^i}(\boldsymbol{x}^{m^i} - \boldsymbol{X}_0^m) \cdot \boldsymbol{N}^i\right] \left\{\boldsymbol{R}^{\mathcal{M}} \cdot [\boldsymbol{1} - \boldsymbol{U}^{\mathcal{M}}] \cdot \boldsymbol{N}^i r^i - \boldsymbol{R}^{\mathcal{M}} \cdot \boldsymbol{N}^i h^i + h^i \boldsymbol{N}^i\right\}.\end{aligned} \tag{10}$$

The corresponding displacement gradient $\boldsymbol{H}^i = \boldsymbol{F}^i - \boldsymbol{1}$ is given by

$$\boldsymbol{H}^{m^i} = \frac{\partial \boldsymbol{u}_{\boldsymbol{x}^{m^i} \in \Omega^i}}{\partial \boldsymbol{x}^{m^i}} = -\left\{\frac{r^{k,i}}{h^i}\left(\frac{\boldsymbol{n}^i}{|\boldsymbol{n}^i|} - \boldsymbol{n}^i\right) + (\boldsymbol{N}^i - \boldsymbol{n}^i)\right\} \otimes \boldsymbol{N}^i \tag{11}$$

with the definitions

$$\boldsymbol{n}^i = \boldsymbol{F}^{\mathcal{M}} \cdot \boldsymbol{N}^i, \tag{12}$$

$$\frac{\boldsymbol{n}^i}{|\boldsymbol{n}^i|} = \boldsymbol{R}^{\mathcal{M}} \cdot \boldsymbol{N}^i. \tag{13}$$

The stress homogenization operator, which translates the stresses of the RVE to the macroscale $\boldsymbol{P}^{\mathcal{M}}$, is a direct outcome of the kinematic coupling operators and the PMVP. This principle, expressed in the reference configuration without considering body forces, ensures that the stress transfer is systematically consistent across different scales

$$V\, \boldsymbol{P}^{\mathcal{M}} : \delta\dot{\boldsymbol{H}}^{\mathcal{M}} \overset{!}{=} \int_\Omega \boldsymbol{P}^m : \delta\dot{\boldsymbol{H}}^m dV. \tag{14}$$

In Equation (14), V denotes the RVE volume. $\boldsymbol{P}^{\mathcal{M}}$ can be represented as a linear mapping of the stresses $\boldsymbol{P}^{m^i}$ of the RVE

$$\boldsymbol{P}^{\mathcal{M}} = \sum_{i=1}^{n} \frac{A^i}{V}\left[h^i \mathbb{I} + \mathbb{I}^{sym}(\boldsymbol{x}^{m^i} - \boldsymbol{X}_0^m) \otimes \boldsymbol{N}^i\right] \boldsymbol{P}^{m^i} = \sum_{i=1}^{n} \mathbb{K}^{m^i} : \boldsymbol{P}^{m^i}. \tag{15}$$

The macroscopic material tangent is obtained by differentiation according to Equation (4)

$$\mathbb{C}^{\mathcal{M}^{\boldsymbol{P}}} = \sum_{i=1}^{n} \mathbb{K}^{m^i} : \frac{d\boldsymbol{P}^{m^i}}{d\boldsymbol{F}^{m^i}} : \frac{\partial \boldsymbol{H}^{m^i}}{\partial \boldsymbol{F}} = \sum_{i=1}^{n} \mathbb{K}^{m^i} : \mathbb{C}^{m^i} : \mathbb{A}^{m^i} \tag{16}$$

with

$$\mathbb{A}^i = \frac{\partial \boldsymbol{H}^i}{\partial \boldsymbol{n}^i} \frac{\partial \boldsymbol{n}^i}{\partial \boldsymbol{F}}. \tag{17}$$

It can be seen that the scale transition from the micro- to the macroscale takes place via the multiplication of linear operators. This enables the linearization required to solve the global system of equations.

3 Mathematical conditions for non-uniform shaped RVE geometries

For the reverse scale transition, the following homogenization operators are used in the context of the PMVP

$$\boldsymbol{u}^{\mathcal{M}} = \frac{1}{V}\int_\Omega \boldsymbol{u}^m \mathrm{d}V, \qquad\qquad \boldsymbol{H}^{\mathcal{M}} = \frac{1}{V}\int_\Omega \boldsymbol{H}^m \mathrm{d}V. \tag{18}$$

They define how the kinematic fields of the microscale are homogenized in order to yield the macroscale point-valued kinematic variables. The required kinematic admissibility of the coupling operators yields the following conditions on the RVE model and its solution

$$\boldsymbol{X}_0^m = \frac{1}{V}\int_\Omega \boldsymbol{X}^m \mathrm{d}V, \qquad \boldsymbol{0} = \int_\Omega \tilde{\boldsymbol{u}}^m \mathrm{d}V \qquad \text{and} \qquad \boldsymbol{0} = \int_\Omega \tilde{\boldsymbol{H}}^m \mathrm{d}V. \tag{19}$$

From the operators defined in Equations (6), (10), (18) and (19), several conditions can be derived for admissible RVE geometries [8]. Since the displacement fields of all deformable layers contain a fluctuation component $\tilde{\boldsymbol{u}}^m$, the first moments of area of the deformable material with respect to $\boldsymbol{X}_0^m$ must vanish

$$\sum_{i=1}^{n} V^i \boldsymbol{r}^i \cdot \boldsymbol{n}^i = \boldsymbol{0}, \tag{20}$$

$$\boldsymbol{T} = \frac{1}{V} \sum_{i=1}^{n} A^i r^i \boldsymbol{n}^i \otimes \boldsymbol{n}^i = \boldsymbol{I}. \tag{21}$$

4 Viscoelastic material model for the microscale

The constitutive relation for the stresses $\boldsymbol{P}^{m^i}$ and deformations $\boldsymbol{F}^{m^i}$ (Equation (3)) at the micro level completes the microlayer framework. If the deformation behaviour of the material is characterised by reversible and irreversible components, as in the phenomenon of viscoelasticity, it is advantageous for the validation of numerical material models by means of experiments if the transient behaviour of the deformation gradient $\dot{\boldsymbol{F}}$, represented by the product of velocity gradient $\boldsymbol{L}$ and deformation gradient $\boldsymbol{F}$

$$\dot{\boldsymbol{F}} = \boldsymbol{L} \cdot \boldsymbol{F}, \tag{22}$$

can be additively split into a purely viscous and a purely elastic part [9]. For this purpose, the deformation gradient is first split multiplicatively into elastic and viscous parts [10]

$$\boldsymbol{F} = \boldsymbol{F}^e \cdot \boldsymbol{F}^v. \tag{23}$$

This creates an intermediate configuration $\mathcal{B}_{tv} \subset \mathcal{B}_t$ in which only viscous deformations are feasible. Many materials additionally exhibit different behaviour under volumetric and isochoric deformations. The deformation gradient is therefore further split into a volume-changing $\boldsymbol{F}_{vol}$ and an unimodular part $\boldsymbol{F}_{iso}$. In several cases, the volumetric part of the deformation gradient is treated as being of secondary importance, and inelastic volumetric components are thus neglected

$$\boldsymbol{F} = \boldsymbol{F}^e_{vol} \cdot \boldsymbol{F}^e_{iso} \cdot \boldsymbol{F}^v_{iso}. \tag{24}$$

The deformation gradient is not a suitable measure for the deformations, as its value also changes with pure rigid body motion. Therefore, the left Cauchy-Green strain tensor

$$\boldsymbol{C} = \frac{1}{2}(\boldsymbol{F}^T \cdot \boldsymbol{F}), \tag{25}$$

$$\boldsymbol{C^e} = \frac{1}{2}(\boldsymbol{F^{e}}^T \cdot \boldsymbol{F^e}) \tag{26}$$

with respect to the initial and intermediate configuration is used. Both tensors have the property of a Riemannian metric with respect to their configuration. The strain energy can therefore be set up in terms of these tensors

$$\psi = \psi^e_{vol}(\boldsymbol{F}) + \psi^e_{iso}(\boldsymbol{C}_{iso}) + \psi^v_{iso}(\boldsymbol{C^e}_{iso}). \tag{27}$$

The purely elastic volumetric part is chosen classically as a function of the bulk modulus $\varkappa$

$$\psi^e_{vol} = \frac{\varkappa}{2}(\ln(\det(\boldsymbol{F})))^2. \tag{28}$$

For the elastic isochoric portion, the Yeoh material model

$$\psi^e_{iso} = \sum_{i=1}^{3} c_i \left(\mathrm{tr}(\boldsymbol{C}_{iso}) - 3\right)^i \tag{29}$$

is used. The computation of the non-equilibrium energy $\psi^v_{iso}(\boldsymbol{C}^e_{iso})$ also starts from the model given in Equation (29). The set of equivalent shear moduli $\tilde{c}_{i,w}$ for each branch w is scaled by

$$\tilde{c}_{i,w} = \alpha_w c_i. \tag{30}$$

In this work, the rheology of the isochoric part is represented by a Maxwell element with two viscous branches ($w = 2$), as shown in Figure 2. With Equation (3), the first Piola-Kirchhoff stress tensor of the elastic component is calculated as

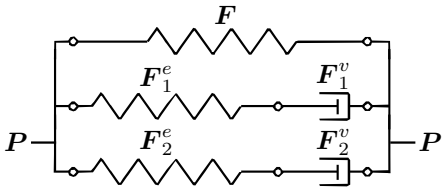

Fig. 2: Rheological approach for modelling viscoelasticity.

$$\boldsymbol{P} = \varkappa(\ln(\det(\boldsymbol{F})))\boldsymbol{F}^{-T} + \frac{\mu}{2}\frac{\partial \mathrm{tr}(\boldsymbol{C}_{iso})}{\partial \boldsymbol{F}_{iso}} : \frac{\partial \boldsymbol{F}_{iso}}{\partial \boldsymbol{F}}. \tag{31}$$

The corresponding material tangent is computed as

$$\begin{aligned}\mathbb{C}^{\boldsymbol{P}} =& \varkappa \left(\boldsymbol{F}^{-T} \otimes \boldsymbol{F}^{-T} + (\ln(\det(\boldsymbol{F})))\frac{\partial \boldsymbol{F}^{-T}}{\partial \boldsymbol{F}} \right) \\ &+\mu \left((\det(\boldsymbol{F}))^{-\frac{2}{3}}\mathbb{I} - \frac{2}{3}\boldsymbol{F}\boldsymbol{F}^{-T}(\det(\boldsymbol{F}))^{-\frac{2}{3}} - \frac{1}{3}\boldsymbol{F}^{-T}\frac{\partial \mathrm{tr}(\boldsymbol{C}_{iso})}{\partial \boldsymbol{F}} - \frac{\mathrm{tr}(\boldsymbol{C}_{iso})}{3}\frac{\partial \boldsymbol{F}^{-T}}{\partial \boldsymbol{F}} \right).\end{aligned} \tag{32}$$

The Neo-Hooke model is also used for $\psi^v(\boldsymbol{C^e}_{iso})$. As a final step, the temporal evolution of the viscous part of Equation (27) is required. The Mandel stress tensor

$$\boldsymbol{\Sigma}^I := 2\boldsymbol{C}^e \cdot \frac{\partial \psi}{\partial \boldsymbol{C}^e} \tag{33}$$

serves as a suitable measure for the evolution, as it is defined in the intermediate configuration and acts as the work-conjugate to the viscous deformations [7]. The velocity gradient of the viscous part is thus a function of the Mandel stress tensor [11]

$$\boldsymbol{L}^v = \dot{\gamma}\boldsymbol{N} = \dot{\gamma}\frac{\mathrm{dev}(\boldsymbol{\Sigma}^{I,v})}{\|\mathrm{dev}(\boldsymbol{\Sigma}^{I,v})\|} \tag{34}$$

with the creep rate

$$\dot{\gamma} = \frac{1}{t_r}\left[\frac{\|\mathrm{dev}(\boldsymbol{\Sigma}^{I,v})\|}{\hat{\Sigma}}\right]. \tag{35}$$

For the application within a numerical simulation, the time evolution of the viscous deformations is solved iteratively according to [12]

$$\boldsymbol{F}^v_{n+1} = \exp\left[\Delta t\dot{\gamma}\boldsymbol{N}\right] \cdot \boldsymbol{F}^v_n. \tag{36}$$

The isochoric part of the viscous Piola Kirchhoff stresses can easily be converted into the Mandel stresses

$$\boldsymbol{\Sigma}^{I,v} = (\boldsymbol{F}^e)^T \cdot \boldsymbol{P}^e \cdot (\boldsymbol{F}^v)^{-T}. \tag{37}$$

5 Numerical examples

5.1 Macroscopic structure and boundary conditions

All simulations are performed on cubical specimens with an edge length of 150 mm and a discretization of four elements per spatial direction. All edge nodes located on the coordinate planes $x_i = 0$ are fixed in their corresponding x_i-direction. A Dirichlet boundary condition is applied to the top surface in the x_3-direction, see Figure 3a. The previously introduced viscoelastic material model with two viscous branches is employed. The parameters of the purely elastic branch as well as the elastic component of the viscoelastic chain w are described using the Yeoh material model. The scalar α_w defines the ratio between the viscoelastic isochoric parameters $\tilde{c}_{p,w}$ and the isochoric elastic parameters c_p.

In the first 50 seconds, a compression state is generated by reducing the height l_3 of the cube linearly by 5 mm using displacement boundary conditions. The direction of the displacements is then changed and the l_3 height of the cube is increased by 10 mm within 100 seconds. In the last time interval of 150 seconds, the l_3 height of the cube is deformed back to the initial height, see Figure 3b. The simulation ends after $t_{tot} = 200$ seconds. The selected material parameters are shown in Table 1.

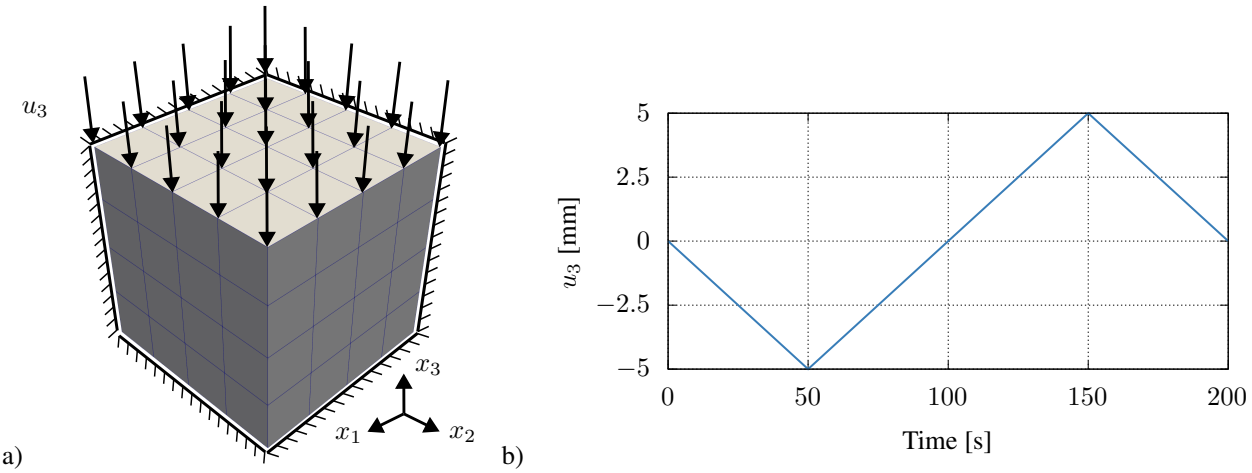

Fig. 3: a) Visualization of the boundary conditions and b) change in the Dirichlet boundary condition u_3 over time

Elastic material parameter	Value	Unit	Viscoelastic material parameter	Value	Unit
$\varkappa$	1000	MPa	α_1	32	[-]
c_1	100	MPa	α_2	2	[-]
c_2	-10	MPa	$t_{r,1}$	28556	s
c_3	1	MPa	$t_{r,2}$	24791	s
$r^{k,i}$	$1-2$	mm	$\hat{\Sigma}_1$	1	MPa
m_{ml}	6	[-]	$\hat{\Sigma}_2$	1	MPa
h^i	0.1	mm			
Simulation parameter					
t_{tot}	200	s			
$\lvert u_{3,max}\rvert$	5	mm			

Table 1: Material parameters for the mulitscale material model for viscoelasticity

5.2 Cuboid-shaped aggregates

A simple cube with a edge length of $r^{k,i}$, onto which deformable microlayers of thickness h^i are imposed on its surfaces, is first introduced as RVE on the microscale. Due to the fact that all corners of the aggregate lie on a spherical shell, the geometry satisfies all requirements of Equation (20). Since the thickness expansion of the microlayer is constant over all layers and small compared to the aggregate edge length, Equation (21) is also approximately fulfilled.

The influence of a rotation α about the x_1-axis on the macroscopic mechanical behavior in loading direction x_3 is first investigated. The results are shown in Figure 4a. Due to the symmetry properties of the cube, the stress–strain curves for $\alpha = 0° \cup 90°$ are identical. In these cases, the magnitudes of the extreme stresses are maximal, as the normal vector of the loaded surface is aligned with the macroscopic loading direction. The relationship between the deformable layers h^i the microscopic deformation measure $\boldsymbol{H}^m$ is inversely proportional (cf. Equation (11))

$$\boldsymbol{H}^m_{\text{extr}} = f\left(\frac{1}{\frac{h^i}{r^{k,i}}}\right). \tag{38}$$

This implies that decreasing values of h^i (or increasing values of $r^{k,i}$) reduces the volume of deformable material at the microstructural level, leading to a higher stress response in a strain controlled setting. Although geometrically, the ratio of aggregate height to layer thickness in the loading direction increases with rotation, the extreme stress values for $\alpha = 22.5° \cup 45°$ are lower. Owing to the simple cube geometry used here, the surface perpendicular to the loading direction is not available, and the load must be distributed across the available surfaces outside the loading direction. Since the microlayers are defined independently and tangential strain components are not transmitted due to modeling simplifications, the resulting low stress peaks are physically inaccurate.

Subsequently, a non-uniform shaped aggregate is generated by doubling the edge lengths in the x_1- and x_2-direction. The corresponding results are shown in Figure 4c. A comparison between $\alpha = 0° \cup 90°$ clearly shows that the anisotropy introduced by the geometry is also reflected in the stress–strain response. At $\alpha = 90°$, the aggregate is loaded along its longest extension, which shifts the extreme stress values to higher levels. Conversely, doubling the layer height h^i in both geometries leads to a reduction of these stress maxima (Figure 4b, d) (cf. Equation (38)). Although the $h^i/r^{k,i}$ ratio is identical for $\alpha = 0°$

in both the cubic geometry (Figure 4a) and the cuboid geometry (Figure 4c), the stress extrema are shifted to higher values in the case of the cuboid. This non-physical increase is due to the fact that the ratio of the base area A^i of a loaded layer i to the total RVE volume V, i.e., A^i/V, also affects the stress homogenization process (cf. Equation (15)). Doubling two of the aggregate edge lengths increases this ratio, since the total base area $A^l = \sum_{j=1}^{l} A^j$ of the actually loaded layer interfaces l increases by a factor of 8, while the overall volume V of the RVE increases by only about a factor of 4.

Assuming the volume ratio A^i/V remains constant, the stress response does not change if the ratio $h^i/r^{k,i}$ is maintained. Therefore, when designing suitable RVE geometries, it is irrelevant whether h^i or $r^{k,i}$ is adjusted.

5.3 Optimized RVE geometry

Based on the insights gained from the cuboid experiment, several requirements and modeling guidelines can be formulated for a physically meaningful, non-inform RVE capable of accurately representing multiaxial stress states. The distorted stress–strain response under loading directions that strongly deviate from the layer normals can be mitigated by introducing large interior angles between adjacent aggregate surfaces. Accordingly, the number of surfaces must increase while the individual surface area decreases.

To satisfy the mathematical constraint equations, canonical polyhedral structures are particularly suitable. The required normal vector geometries and surface-related geometric quantities needed to solve the RVE problem Equation (11) are well documented in the literature [13, 14] and available in various programming libraries. For extending the concept to geometrically non-uniform RVE structures, it is therefore not only physically meaningful but also more practical to vary the layer thickness rather than the aggregate geometry itself. This is illustrated by another numerical example. Using the Python library `trimesh` [15], the faces of an icosahedron are first subdivided by double triangulation. The resulting 320 triangular faces are then projected onto a spherical surface with $r^{k,i} = 1$ mm to form an icosphere. Due to the inherent point symmetry, Equation (20) is automatically satisfied. Furthermore, the symmetry of the icosahedron allows only half of the faces to be considered. The layer thickness is set to $h^i = t$ on surfaces perpendicular to the x_1- and x_2-direction. To introduce geometric anisotropy, a larger value of $h^i = 2t$ is assigned to the surface perpendicular to the x_3-direction. Between these values, a linear interpolation is applied. Since the layer height now varies, Equation (21) is initially not satisfied. However, by solving Equation (21) iteratively, the value of t can be determined as

$$t = 0.308 \text{ mm}. \tag{39}$$

The resulting polyhedron and its imposed layers are shown in Figure 5a. Figure 5b displays the corresponding stress–strain response for the numerical experiment described in Section 5.1. Compared to the cube-based RVEs, the extreme stress values are noticeably reduced, as the $h^i/r^{k,i}$ ratio increases while the A^i/V ratio decreases. The influence of anisotropy is clearly observable but appears relatively weaker due to the increased amount of deformable material. In contrast to the cube-shaped RVEs, the relation between decreasing $h^i/r^{k,i}$ and increasing stress maxima is now qualitatively captured: With increasing rotation around the x_1-axis, the stress extrema rise accordingly. This is ensured by maintaining a constant A^i/V ratio and increasing the number of microlayer. The chosen geometry is thus well-suited to produce a meaningful stress response under geometrically induced anisotropy.

6 Conclusion

In the present work, selected numerical examples are used to systematically derive both mathematical and physical requirements for the geometry of the representative volume element within the microlayer framework. As a result, this study provides foundational strategies for the design and realization of explicit material microstructures. Future work should investigate alternative polyhedral structures with the dual aim of reducing the number of required polyhedral faces to improve numerical efficiency, and enabling a broader and more flexible choice of the $h^i/r^{k,i}$ ratio while still satisfying Equation (21).

Acknowledgements The present work has been developed under the research project No. 453596084 (SFB/TRR 339, Project A01) and under project No. 414936990 (KA 1163/46-2), which has been granted by the German Research Foundation (Deutsche Forschungsgemeinschaft). This financial support is gratefully acknowledged.

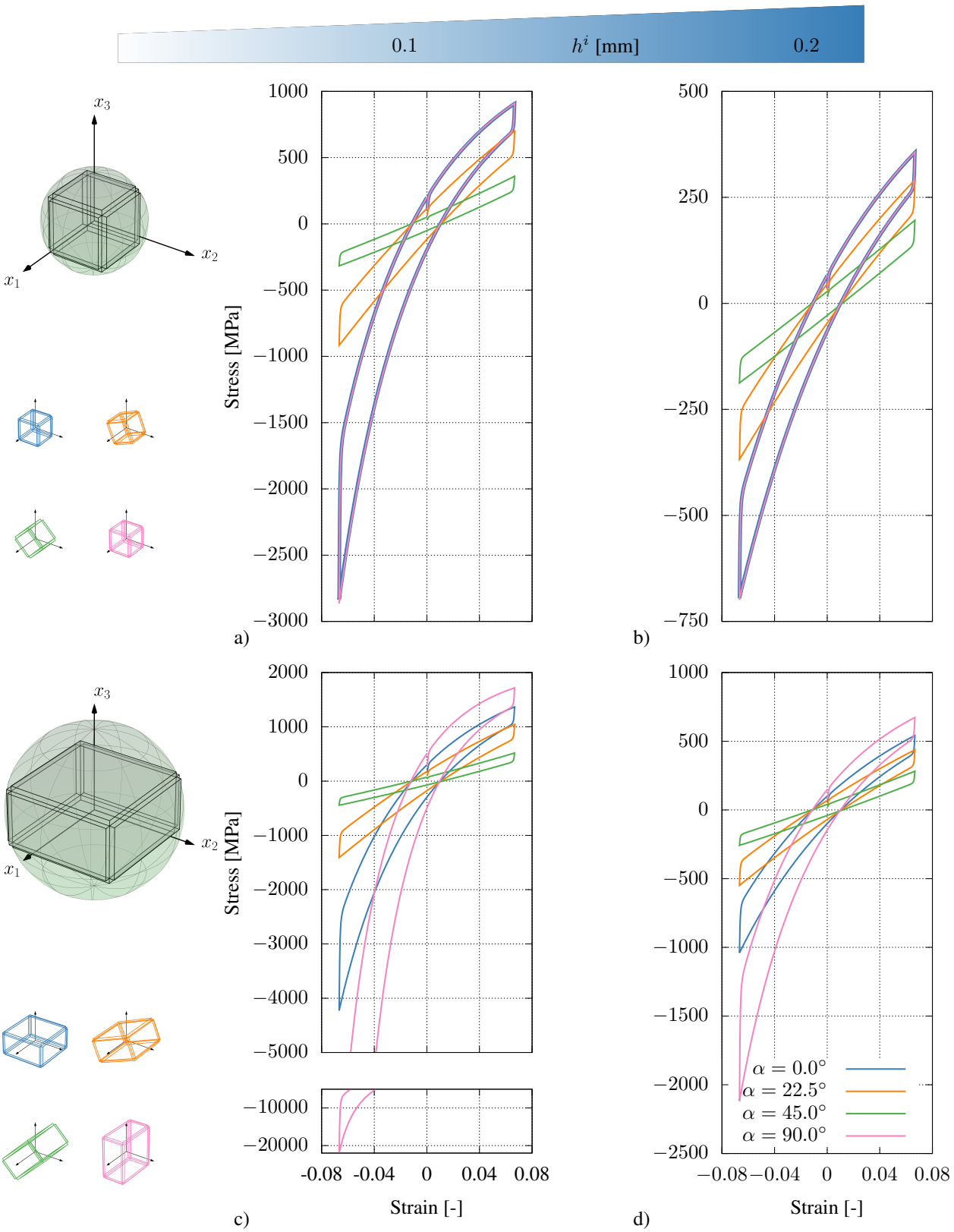

Fig. 4: Viscoelastic hysteresis in loading direction x_3 for four different rotation angles α of the aggregates about the x_1-axis. The results are shown with increasing anisotropy, achieved by increasing the radius ratio $r^{k,1,2}/r^{k,3}$ (top to bottom), and by increasing the layer thickness through a higher ratio of $h^i/r^{k,i}$ (left to right).

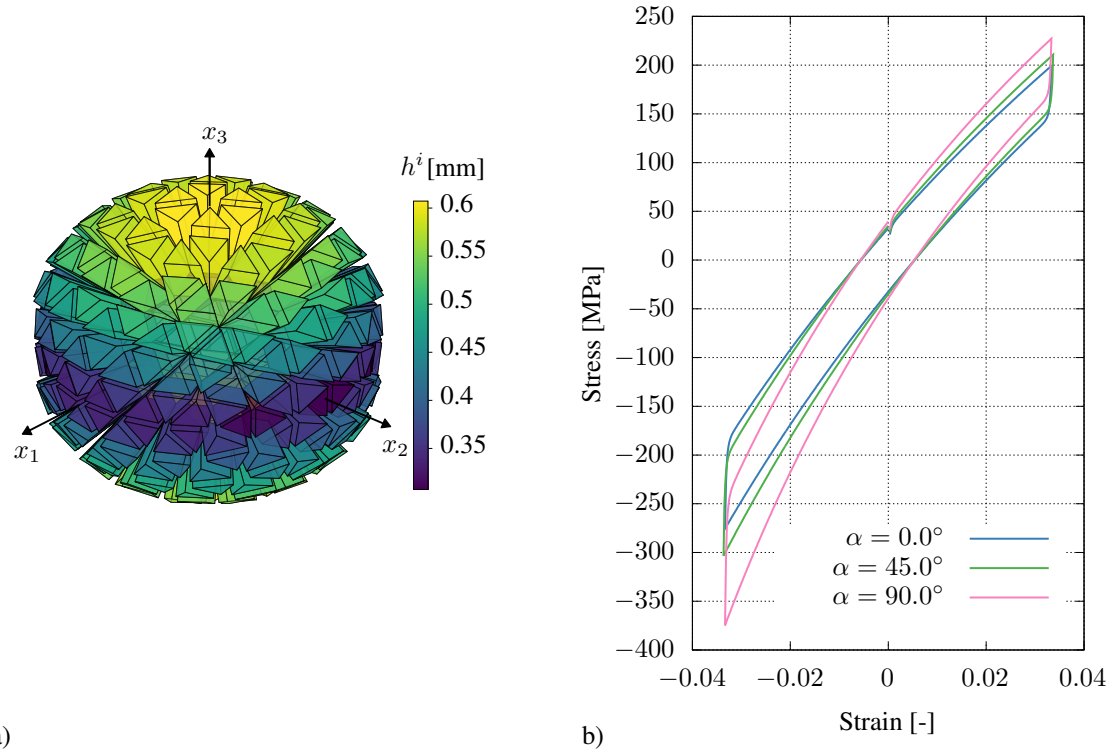

a) b)

Fig. 5: a) RVE geometry with varying layer height h^i, and b) the associated stress–strain hysteresis in loading direction for selected rotation angles α around the x_1-axis

References

[1] A. Zeißler, Untersuchungen zum spannungsabhängigen Materialverhalten von Asphalt (Habilitation thesis, Institut für Stadtbauwesen und Verkehr, Technische Universität Dresden, 2015).

[2] S. Schmidt, M. Wiebicke, and I. Herle, E3S Web of Conferences **544**, 04003 (2024).

[3] M. Schumacher, A. Lode, A. Helth, and M. Gelinsky, Acta Biomaterialia **9**, 9547–9557 (2013).

[4] H. Böhm, A. Eckschlager, and W. Han, Computational Materials Science **25**, 42–53 (2002).

[5] J. Platen, J. Storm, S. Bosbach, M. Claßen, and M. Kaliske, Computers & Structures **293**, 107258 (2024).

[6] P. J. Blanco, P. J. Sánchez, E. A. de Souza Neto, and R. A. Feijóo, Archives of Computational Methods in Engineering **23**, 191–253 (2016).

[7] J. Platen, B. Pauls, A. Anantheswar, T. Lautenschläger, C. Neinhuis, and M. Kaliske, International Journal for Numerical Methods in Engineering **125**, e7483 (2024).

[8] J. Storm and M. Kaliske, Proceedings in Applied Mathematics and Mechanics **18**, e201800364 (2018).

[9] C. Miehe, Kanonische Modelle multiplikativer Elasto-Plastizität: thermodynamische Formulierung und numerische Implementation (Habilitation thesis, Institut für Baumechanik und Numerische Mechanik, Universität Hannover, 1993).

[10] J. Platen, I. Zreid, and M. Kaliske, International Journal of Solids and Structures **267**, 112151 (2023).

[11] H. Dal and M. Kaliske, Computational Mechanics **44**, 809–823 (2009).

[12] G. Weber and L. Anand, Computer Methods in Applied Mechanics and Engineering **79**, 173–202 (1990).

[13] H. S. M. Coxeter, Regular polytopes, 3rd edition (Dover Publ., New York, 1973).

[14] B. Grünbaum, V. Kaibel, V. Klee, and G. M. Ziegler, Convex polytopes, 2nd edition (Springer, Heidelberg, 2003).

[15] M. Dawson-Haggerty et al., Trimesh python library, https://trimesh.org, (Last accessed on 22 July 2025).